Epigenetic loss of the endoplasmic reticulum–associated degradation inhibitor SVIP induces cancer cell metabolic reprogramming

Pere Llinàs-Arias,[1,2] Margalida Rosselló-Tortella,[1] Paula López-Serra,[1] Montserrat Pérez-Salvia,[1,2] Fernando Setién,[1] Silvia Marin,[3,4,5] Juan P. Muñoz,[3,6,7] Alexandra Junza,[7,8] Jordi Capellades,[7,8] María E. Calleja-Cervantes,[1] Humberto J. Ferreira,[1] Manuel Castro de Moura,[1] Marina Srbic,[1] Anna Martínez-Cardús,[1] Carolina de la Torre,[9] Alberto Villanueva,[10] Marta Cascante,[3,4,5] Oscar Yanes,[7,8] Antonio Zorzano,[3,6,7] Catia Moutinho,[1,11] and Manel Esteller[1,2,12,13,14]

[1]Cancer Epigenetics Group, Cancer Epigenetics and Biology Program (PEBC), Bellvitge Biomedical Biomedical Research Institute (IDIBELL), Barcelona, Catalonia, Spain. [2]Centro de Investigacion Biomedica en Red Cancer (CIBERONC), Madrid, Spain. [3]Department of Biochemistry and Molecular Biomedicine, Faculty of Biology, University of Barcelona, Barcelona, Spain. [4]Institute of Biomedicine of Universitat de Barcelona (IBUB), Barcelona, Spain. [5]CIBER of Liver and Digestive Diseases (CIBEREHD), Madrid, Spain. [6]Institute for Research in Biomedicine (IRB Barcelona), Barcelona Institute of Science and Technology, Barcelona, Spain. [7]CIBER of Diabetes and Associated Metabolic Diseases (CIBERDEM), Madrid, Spain. [8]Metabolomics Platform, IISPV, Department of Electronic Engineering (DEEEA), Universitat Rovira i Virgili, Tarragona, Catalonia, Spain. [9]Proteomics Unit, Bellvitge Biomedical Research Institute (IDIBELL), L'Hospitalet, Barcelona, Catalonia, Spain. [10]Translational Research Laboratory, Catalan Institute of Oncology (ICO), Bellvitge Biomedical Research Institute (IDIBELL), L'Hospitalet, Barcelona, Catalonia, Spain. [11]CNAG-CRG, Centre for Genomic Regulation (CRG), Barcelona Institute of Science and Technology (BIST), Barcelona, Spain. [12]Josep Carreras Leukaemia Research Institute (IJC), Badalona, Barcelona, Catalonia, Spain. [13]Institució Catalana de Recerca i Estudis Avançats (ICREA), Barcelona, Catalonia, Spain. [14]Physiological Sciences Department, School of Medicine and Health Sciences, University of Barcelona, Catalonia, Spain.

The endoplasmic reticulum (ER) of cancer cells needs to adapt to the enhanced proteotoxic stress associated with the accumulation of unfolded, misfolded, and transformation-associated proteins. One way by which tumors thrive in the context of ER stress is by promoting ER-associated degradation (ERAD), although the mechanisms are poorly understood. Here, we show that the small p97/VCP-interacting protein (SVIP), an endogenous inhibitor of ERAD, undergoes DNA hypermethylation–associated silencing in tumorigenesis to achieve this goal. SVIP exhibits tumor suppressor features and its recovery is associated with increased ER stress and growth inhibition. Proteomic and metabolomic analyses show that cancer cells with epigenetic loss of SVIP are depleted in mitochondrial enzymes and oxidative respiration activity. This phenotype is reverted upon SVIP restoration. The dependence of SVIP-hypermethylated cancer cells on aerobic glycolysis and glucose was also associated with sensitivity to an inhibitor of the glucose transporter GLUT1. This could be relevant to the management of tumors carrying SVIP epigenetic loss, because these occur in high-risk patients who manifest poor clinical outcomes. Overall, our study provides insights into how epigenetics helps deal with ER stress and how SVIP epigenetic loss in cancer may be amenable to therapies that target glucose transporters.

Introduction

The growth and survival of cancer cells in the context of many cell-intrinsic and cell-extrinsic stresses, such as nutrient deprivation or hypoxia, relies upon balanced protein synthesis, folding, quality control, and degradation. The accelerated protein synthesis rate and the rapid cell cycle of these transformed cells make them even more dependent on correct protein homeostasis. This observation has been explored in a therapeutic context where proteasome inhibitors, which drive cancer cells into a state of proteotoxic stress, have been successful in

treating certain hematologic malignancies (1). The endoplasmic reticulum (ER) is a critical organelle in protein homeostasis that, in addition to lipid synthesis and distribution, and calcium regulation (2), controls protein synthesis, folding, modification, and transport. In this regard, nearly one-third of all cellular proteins are synthesized, folded, and modified in the ER (3). If, at steady state, the ER is able to maintain protein homeostasis, the high protein synthesis rate and the increased number of misfolded proteins that occur in cancer cells can trigger an ER stress response that will eventually lead to apoptosis (3). Thus, tumors must adapt their ER machinery to handle this proteotoxic stress if they are to survive and keep growing. The main ER stress adaptive mechanisms are the unfolded protein response (UPR) and the ER-associated degradation (ERAD) pathways (4). Both of them lead to global protein attenuation and the clearance of misfolded proteins in the ER to ameliorate the proteotoxic stress. The UPR network in the context of human tumors has been widely studied (5), and here we focus more on the ERAD pathway, which is less well understood at the molecular level.

ERAD ensures protein quality and quantity by guiding misfolded or unassembled proteins from the ER to their degradation by the ubiquitin-proteasome system (UPS) (6). ERAD is also used to regulate the excessive abundance of mature proteins in response to shifts in cellular requirements (6). The ERAD substrates are retrotranslocated across the ER membrane into the cytosol through the AAA-ATPase valosin-containing protein (VCP, also known as p97) and degraded by the 26S proteasome (6). The key role of VCP in protein homeostasis is highlighted by the observation that its specific inhibitors lead to irresolvable proteotoxic stress associated with antitumor activity (7–9), even in cancer models where proteasome inhibitors are inactive (7), a finding that prompted their further evaluation in clinical trials (ClinicalTrials.gov identifiers: NCT02243917 and NCT02223598). Thus, the activity of VCP in cells must be tightly regulated. In this regard, there are 3 proteins that possess a VCP-interacting motif (VIM) (10) that allows them to bind directly to VCP: E3 ubiquitin-protein ligase AMFR (also known as tumor autocrine motility factor receptor, or gp78) (11); selenoprotein S (also known as SELENOS or VIMP) (12), which acts as a recruitment factor for E3 ubiquitin-protein ligase synoviolin (SYVN1 or HRD1) (13); and small VCP/p97-interacting protein (SVIP). AMFR and SELENOS-SYVN1 promote ERAD due to their catalytic activity and interaction with DERL proteins (11), while SVIP acts as an endogenous inhibitor of this process (14).

We wondered about the existence of cancer-specific defects in VCP and its main interactor proteins that could explain how tumoral ER can maintain protein homeostasis to overcome cell death. We found that SVIP behaves as a tumor suppressor gene that undergoes epigenetic-associated transcriptional silencing in a wide range of human tumors. SVIP restoration in deficient cells blocks ERAD, promotes ER stress, and induces a metabolic shift from aerobic glycolysis to mitochondrial respiration. Our findings thus indicate a role for SVIP loss as an adaptive mechanism in human tumors to thrive in the ER stress–prone environment of cancer cells.
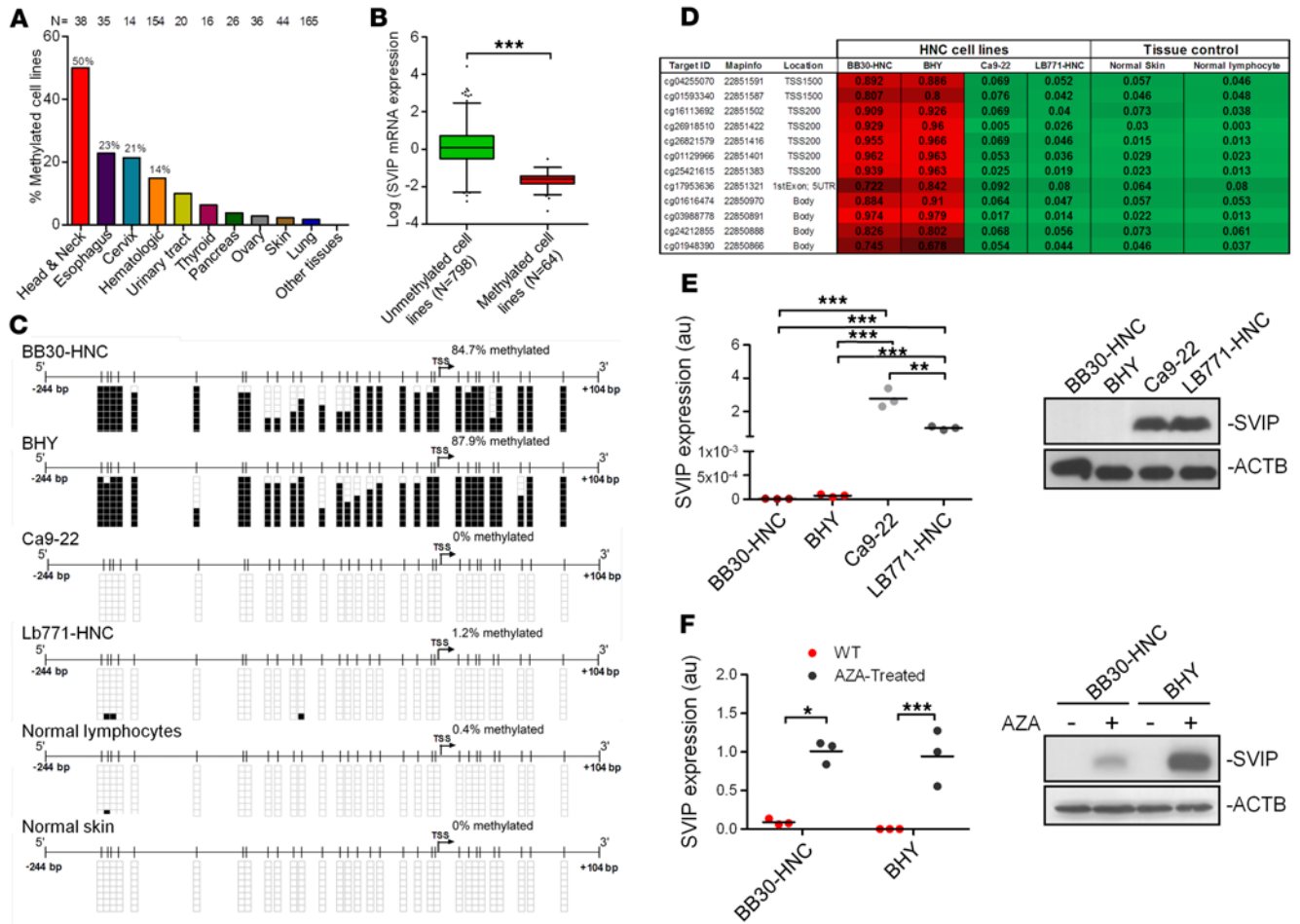
Results

Characterization of SVIP CpG island promoter hypermethylation–associated transcriptional silencing in cancer cells. To find putative genetic and epigenetic changes in the VCP-mediated ERAD pathway composed of VCP, SELENOS, SYVN1, SVIP, AMFR, and DERLIN1-3 in human tumors, we first data-mined a set of 1,001 human cancer cell lines in which we had recently obtained the exome sequence, transcriptome, gene copy number, and DNA methylation landscapes (15). The status of DERLIN1-3 in this collection of samples has previously been studied (16) and is not discussed further here. The available genomic data did not show the existence of VCP, SELENOS, SYVN1, SVIP, and AMFR mutations, deletions, or amplifications in the analyzed cell lines (Supplemental Dataset 1; supplemental material available online with this article; https://doi.org/10.1172/jci.insight.125888DS1). Although no genetic lesions were observed in the aforementioned genes, transcriptional silencing by promoter CpG island hypermethylation is an alternative mechanism by which gene inactivation in transformed cells may be achieved (17–19). VCP/p97, SELENOS, SYVN1, and AMFR/GP78 promoter-associated CpG islands were unmethylated in the analyzed cell lines (Supplemental Dataset 1). However, the SVIP promoter CpG island was methylated in 50% (19 of 38) of head and neck cancer cell lines (Figure 1A and Supplemental Dataset 1). Apart from head and neck tumors, the SVIP promoter CpG island was most often found to be unmethylated in the other cancer types, with the exception of esophageal (8 of 35, 23%) and cervical (3 of 14, 21%) cancers, and hematological malignancies (22 of 154, 14%), particularly B cell lymphoma (15 of 45, 33%) (Figure 1A and Supplemental Dataset 1). Data-mining of the available transcriptome profiles in this cancer cell line collection (15) showed SVIP hypermethylation to be associated with downregulation of the mRNA (Figure 1B and Supplemental Figure 1A). The SVIP promoter CpG island was found to be unmethylated in all the normal human tissues tested (Supplemental Dataset 2).

Having observed the SVIP CpG island methylation profiles described above, we interrogated in detail the link with the loss of the SVIP gene at the RNA and protein levels. We performed bisulfite genomic sequencing of multiple clones in head and neck (BB30-HNC, BHY, Ca9-22, and LB771-HNC), esophageal (COLO-680N, KYSE-180, and OACM 5.1C), and cervical (Ca-Ski, HeLa, and SW756) cancer cell lines using oligonucleotides that encompassed the transcription start site–associated CpG island. We observed that the 5′-end CpG island of SVIP in the BB30-HNC, BHY, COLO-680N, KYSE-180, and Ca-Ski cell lines was hypermethylated in comparison with normal tissues (Figure 1C and Supplemental Figure 1B), whereas the Ca9-22, LB771-HNC, OACM 5.1C, HeLa, and SW756 and cells were unmethylated (Figure 1C and Supplemental Figure 1B). These results mimicked DNA methylation profiles determined using the microarray approach (Figure 1D and Supplemental Figure 1C). The SVIP-hypermethylated cell lines BB30-HNC, BHY, COLO-680N, KYSE-180, and Ca-Ski minimally expressed the SVIP RNA transcript and protein, as determined by quantitative PCR (qPCR) and Western blot, respectively (Figure 1E and Supplemental Figure 1D). Expression of SVIP RNA and protein was observed in the unmethylated cell lines (Figure 1E and Supplemental Figure 1D). Treatment of the SVIP-methylated cell lines with the DNA methylation inhibitor 5-aza-2′-deoxycytidine restored SVIP expression (Figure 1F and Supplemental Figure 1E). In summary, these data indicate that tumor-specific promoter CpG island hypermethylation–associated silencing of the SVIP gene takes place in cancer cells.

SVIP exhibits tumor suppressor features. Once we had shown the presence of SVIP CpG island hypermethylation–associated loss in cancer cell lines, we assessed its role in tumor growth in vitro and in vivo. We first studied the effect of the recovery of SVIP expression in epigenetically silenced cells. Upon the efficient transfection of SVIP in the hypermethylated BB30-HNC cells, validated by qPCR and Western blot (Figure 2A), we found a significant reduction in cellular growth measured by the sulforhodamine B (SRB) assay in comparison with empty vector–transfected cells (Figure 2B). We extended the model to a second head and neck cancer cell line, one cervical cancer cell line, and two esophageal cancer cell lines where we also found that the efficient recovery of SVIP expression by transfection in the SVIP-hypermethylated BHY, Ca-Ski, COLO-680N, and KYSE-180 cells (Supplemental Figure 2A) induced a significant reduction in cell viability (Supplemental Figure 2B). We also developed the reverse approach by studying the effect of SVIP depletion in head and neck cancer cells that were unmethylated and expressed the SVIP transcript and protein. Upon efficient short hairpin RNA–mediated (shRNA-mediated) depletion of SVIP in Ca9-22 cells, validated by qPCR and Western blot (Figure 2C), we observed that the reduction of SVIP levels had growth-promoting features, determined by an increased viability in the SRB assay, in comparison with scramble shRNA–treated cells (Figure 2D). In this regard, low levels of SVIP are also associated with high expression of the proliferation marker CCND1 in the Sanger panel of cancer cell lines (15) (Supplemental Figure 2C).

The in vitro data were then interrogated in an in vivo model. We studied the capacity of SVIP-transfected BB30-HNC cells to form subcutaneous tumors in nude mice compared with empty vector–transfected cells. The recovery of SVIP expression in these head and neck tumors decreased their growth in comparison with empty vector–derived tumors, as shown by the continuous measurement of the tumor volume (Figure 2E). Tumor samples obtained at the endpoint of the experimental model showed that tumors of the SVIP-transfected cells weighed less than those measured in empty vector–transfected cells (Figure 2E). Overall, our observations indicate that SVIP has tumor suppressor–like properties in cancer cells.

SVIP promotes ER stress, rendering cancer sells sensitive to SERCA inhibition. Once we had determined the epigenetic silencing of SVIP in cancer cells and its role in promoting tumor growth, we turned our attention to the effect of SVIP expression on ER stress. In this regard, it has previously been shown that prolonged ER stress, usually associated with the accumulation of misfolded protein in the ER, is associated with SVIP overexpression (14, 20, 21). For this reason, we assessed the cellular and molecular phenotypes of the ER in our experimental model. Using transmission electron microscopy (TEM), we found that the restoration of SVIP expression in the hypermethylated BB30-HNC, BHY, and Ca-Ski cells induced the formation of intracellular vacuoles derived from the ER, indicated by the presence of attached ribosomes, in comparison with what occurred in empty vector–transfected cells (Figure 3A and Supplemental Figure 3A). Similar vacuolation and ER dilation has already been described as a consequence of SVIP transfection in other models (22). These vacuoles are thought to be caused by the accumulation of misfolded proteins (23). Most importantly, we found that the recovery of SVIP expression in the hypermethylated head and neck (BB30-HNC and BHY) and cervical (Ca-Ski) cancer cells provoked not only cell vacuolation, but also overall upregulation of proteins associated with ER stress (Figure 3B and Supplemental Figure 3B). This was the

Target ID	Mapinfo	Location	HNC cell lines				Tissue control	
			BB30-HNC	BHY	Ca9-22	LB771-HNC	Normal Skin	Normal lymphocyte
cg04255070	22851591	TSS1500	0.892	0.886	0.069	0.052	0.057	0.046
cg01593340	22851587	TSS1500	0.807	0.8	0.076	0.042	0.046	0.048
cg16113692	22851502	TSS200	0.909	0.926	0.069	0.04	0.073	0.038
cg26918510	22851422	TSS200	0.929	0.96	0.005	0.026	0.03	0.003
cg26821579	22851416	TSS200	0.955	0.966	0.069	0.046	0.015	0.013
cg01129966	22851401	TSS200	0.962	0.963	0.053	0.036	0.029	0.023
cg25421615	22851383	TSS200	0.939	0.963	0.025	0.019	0.023	0.013
cg17953636	22851321	1stExon; 5UTR	0.722	0.842	0.092	0.08	0.064	0.08
cg01616474	22850970	Body	0.884	0.91	0.064	0.047	0.057	0.053
cg03988778	22850891	Body	0.974	0.979	0.017	0.014	0.022	0.013
cg24212855	22850888	Body	0.826	0.802	0.068	0.056	0.073	0.061
cg01948390	22850866	Body	0.745	0.678	0.054	0.044	0.046	0.037

Figure 1. Transcriptional silencing of *SVIP* by promoter CpG island hypermethylation in human cancer cells. (A) Percentage of *SVIP* methylated cell lines in the Sanger panel of cancer cell lines by tumor type. Cell lines were considered methylated if the average of β values of interrogated CpGs was equal to or higher than 0.66. **(B)** *SVIP* promoter CpG island hypermethylation is significantly associated with loss of the *SVIP* transcript in the Sanger cancer cell lines (n = 862). **(C)** Bisulfite genomic sequencing of *SVIP* promoter CpG island in head and neck cancer cell lines, normal lymphocytes, and normal skin. CpG dinucleotides are represented as short vertical lines; the transcription start site (TSS) is represented as a long black arrow. Single clones are shown for each sample. Presence of an unmethylated or methylated cytosine is indicated by a white or black square, respectively. **(D)** DNA methylation profile of the CpG island promoter for the *SVIP* gene analyzed by the 450K DNA methylation microarray. Single CpG absolute methylation levels (0–1) are shown. Green, unmethylated; red, methylated. Data from the 4 head and neck cancer cell lines, normal lymphocytes, and normal skin are shown. **(E)** SVIP expression levels in head and neck cancer cell lines determined by qPCR (data shown represent the mean biological triplicates) (left) and Western blot (right). **(F)** Expression of the SVIP RNA transcript (data shown represent the mean of biological triplicates) (left) and protein (right) was restored in the *SVIP* epigenetically silenced BB30-HNC and BHY cells by treating with the demethylating drug 5-aza-2′-deoxycytidine (AZA). qPCRs were analyzed using a 2-tailed Student's *t* test. *P < 0.05; **P < 0.01; ***P < 0.001.

case for those proteins involved in the unfolded protein response (UPR), such as IRE1α (total and phosphorylated), PERK, BIP, and phosphorylated eIF2α, and those involved in protein folding, such as PDI and ERO1-Lα (Figure 3B and Supplemental Figure 3B). In agreement with the observed phenotype, the shRNA-mediated depletion of SVIP in the unmethylated Ca9-22 induced the opposite effect: the downregulation of the described UPR and protein folding markers (Figure 3B). Data mining of the Sanger panel of cancer cell lines further confirmed that SVIP hypermethylation was associated with the overexpression of other ER stress markers such as the UPR protein XBP1 and the ERAD protein DERL3 (Supplemental Figure 3C). SVIP restoration did not affect Sel1L and Hrd1 levels (Supplemental Figure 3D). Autophagy was also induced upon SVIP transfection in BB30-HNC cells, as demonstrated by the presence of double-membrane autophagosomes (Figure 3A) and the induction of the autophagy-related proteins BECLIN1 and p62, in addition to the cleavage of LC3B (Figure 3C). The recovery of SVIP expression in these cancer cells was not associated with the formation of apoptotic bodies (Figure 3A), the cleavage of the proapoptotic proteins PARP and caspase 3 (Figure 3D), or the induction of cell cycle arrest or senesce determined by
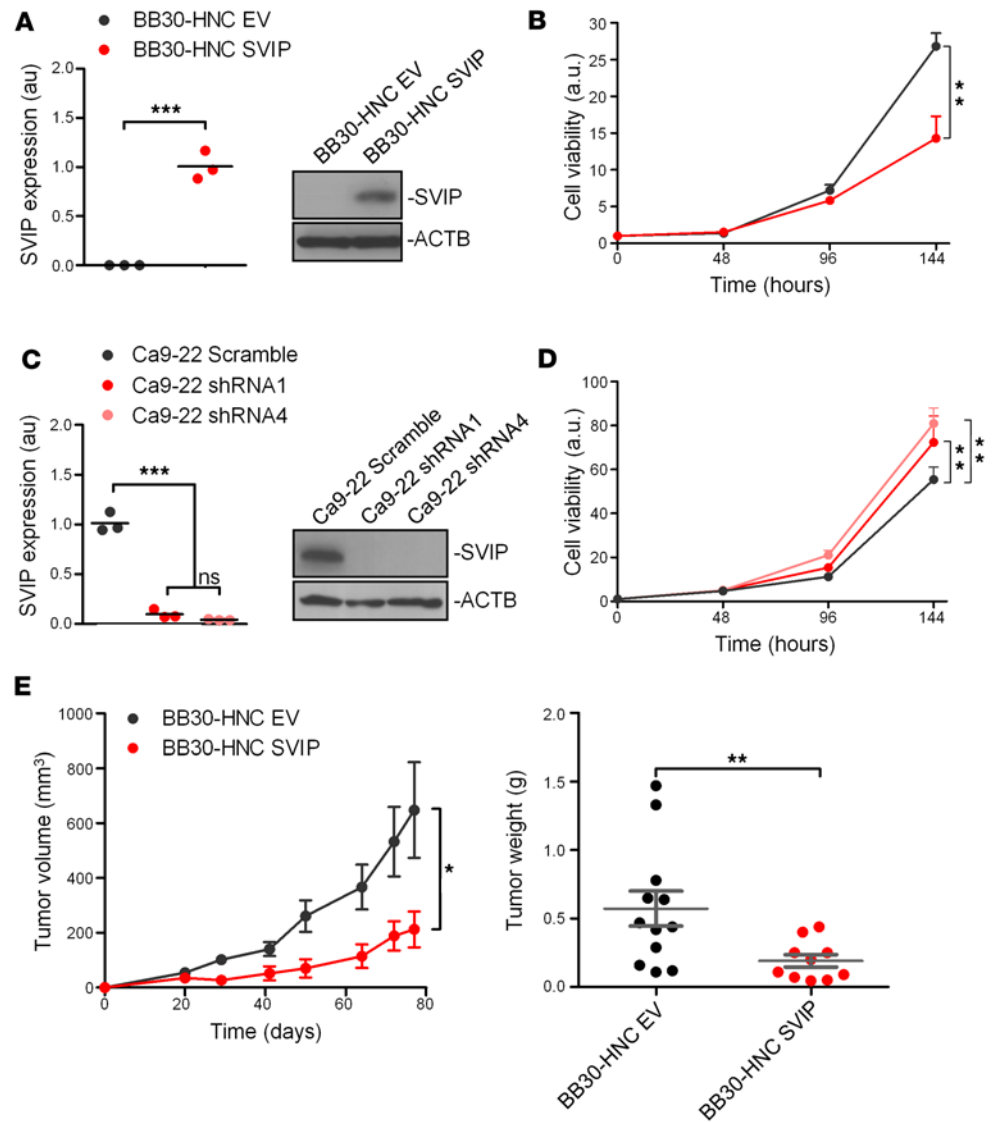
Figure 2. SVIP features tumor suppressor activities in vitro and in vivo. (**A**) Efficient restoration of SVIP expression upon transfection in BB30-HNC cells according to qPCR (left) and Western blot (right). qPCR values are represented as mean of biological triplicates and analyzed using a 2-tailed Student's *t* test. (**B**) SRB assay shows that SVIP transfection reduces viability of BB30-HNC cells. This graph is representative of 3 independent experiments. Each data point represents mean ± SD. Statistical differences were determined using a 2-tailed Student's *t* test at the 144-hour time point. (**C**) Efficient shRNA-mediated depletion of SVIP according to qPCR (left) and Western blot (right) in the unmethylated Ca9-22 head and neck cancer cell line. qPCR values are represented as mean of biological triplicates and analyzed using a 2-tailed Student's *t* test. Two shRNA clones are shown. (**D**) SRB assay shows that SVIP shRNA-mediated depletion increases viability of Ca9-22 cells. This graph is representative of 3 independent experiments. Each data point represents mean ± SD. Statistical differences were determined using a 2-tailed Student's *t* test at the 144-hour time point. (**E**) Empty vector–transfected (EV-transfected) and SVIP-transfected BB30-HNC cells were injected into the left and right flank, respectively, of 10 mice. Tumor volume over time (left) and tumor weight upon sacrifice (right) are shown. Tumor growth and weight were analyzed using a 2-tailed Student's *t* test. Data shown as mean ± SEM. *$P < 0.05$; **$P < 0.01$; ***$P < 0.001$. ns, not significant.

p21 immunoblotting (Figure 3E) and the senescence-associated β-galactosidase assay (Supplemental Figure 3E), respectively. Thus, these data suggest that SVIP epigenetic silencing could be used in cancer cells as a way of reducing ER stress and maintaining the protein homeostasis that is necessary for their survival.

Pharmacological agents that induce ER stress have been found to exhibit antitumor activity. Thus, we also examined whether cells that experience enhanced ER stress upon SVIP transfection can be pushed over the edge by these drugs because they can no longer cope with the massive ER stress levels. We did not detect any

JCI insight
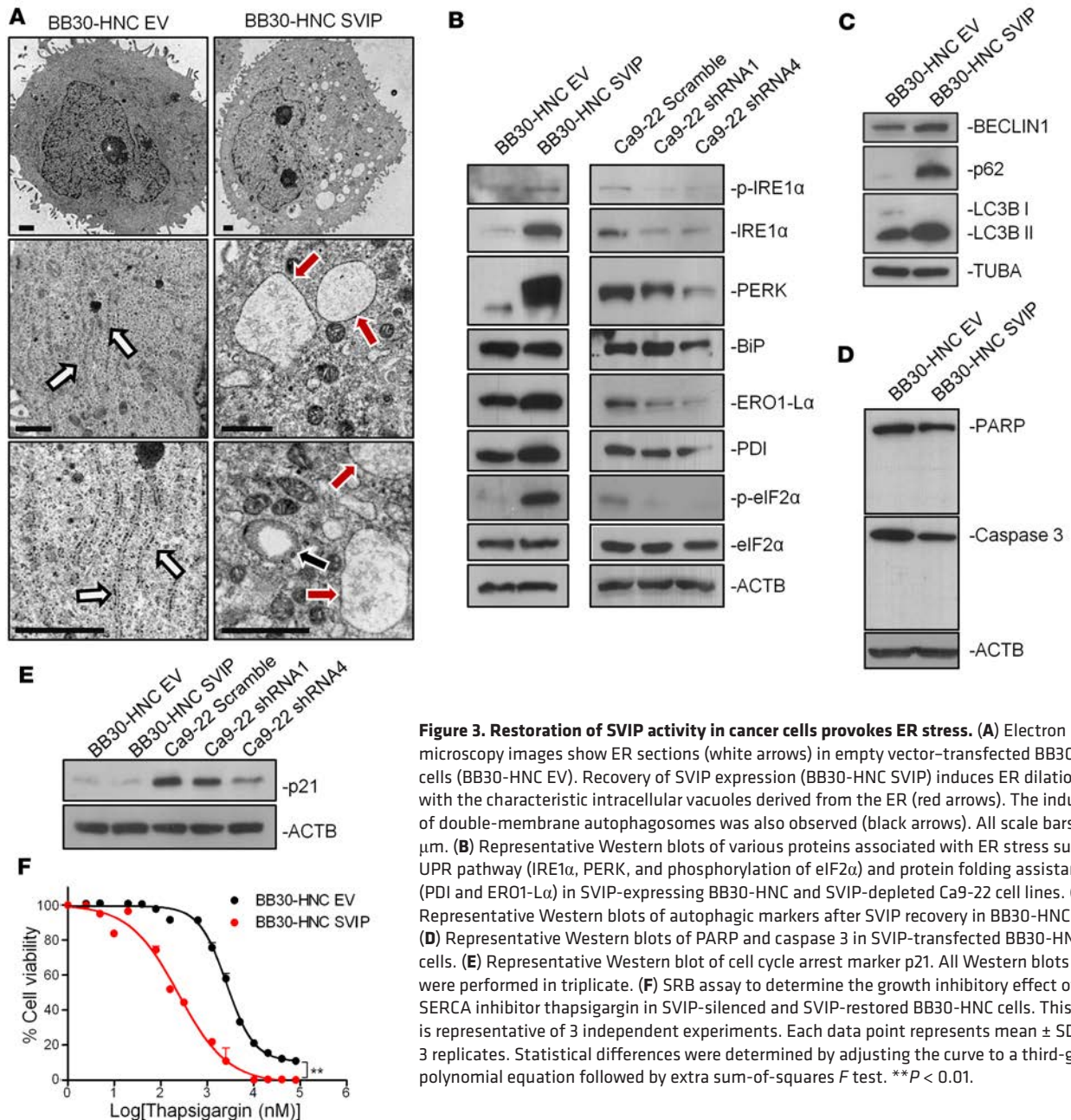
Figure 3. Restoration of SVIP activity in cancer cells provokes ER stress. (A) Electron microscopy images show ER sections (white arrows) in empty vector–transfected BB30-HNC cells (BB30-HNC EV). Recovery of SVIP expression (BB30-HNC SVIP) induces ER dilation with the characteristic intracellular vacuoles derived from the ER (red arrows). The induction of double-membrane autophagosomes was also observed (black arrows). All scale bars: 1 μm. **(B)** Representative Western blots of various proteins associated with ER stress such as UPR pathway (IRE1α, PERK, and phosphorylation of eIF2α) and protein folding assistance (PDI and ERO1-Lα) in SVIP-expressing BB30-HNC and SVIP-depleted Ca9-22 cell lines. **(C)** Representative Western blots of autophagic markers after SVIP recovery in BB30-HNC cells. **(D)** Representative Western blots of PARP and caspase 3 in SVIP-transfected BB30-HNC cells. **(E)** Representative Western blot of cell cycle arrest marker p21. All Western blots in **B**–**E** were performed in triplicate. **(F)** SRB assay to determine the growth inhibitory effect of the SERCA inhibitor thapsigargin in SVIP-silenced and SVIP-restored BB30-HNC cells. This graph is representative of 3 independent experiments. Each data point represents mean ± SD of 3 replicates. Statistical differences were determined by adjusting the curve to a third-grade polynomial equation followed by extra sum-of-squares F test. **$P < 0.01$.

difference in cell viability, measured by the SRB assay, between SVIP- and empty vector–transfected BB30-HNC cells upon the use of proteasome (bortezomib) (24), VCP/p97 (Eeyarestatin I and NMS-873) (25, 26), and Hsp90 (17-AAG and IPI-504) (27, 28) inhibitors (Supplemental Figure 4). However, the recovery of SVIP expression in these cancer cells rendered them sensitive to thapsigargin (Figure 3F), a specific inhibitor of the sarcoplasmic/ER Ca^{2+}-ATPase (SERCA) (29). SERCA is responsible for calcium transference from the cytosol to ER, and low levels of calcium in the ER are associated with the loss of activity of calcium-dependent ER chaperones, such as calnexin and calreticulin, leading to the accumulation of unfolded proteins (30, 31). These results are further evidence of the role of SVIP in inducing ER stress in cancer cells, and suggest that they could be targeted by compounds that disturb calcium homeostasis.

SVIP induces a metabolic shift from aerobic glycolysis to mitochondrial respiration. The impact of SVIP on ER stress is linked to the role of SVIP as an endogenous inhibitor of ERAD (14). The ER is a central organelle for the synthesis and maturation of proteins, and the ERAD pathway eliminates misfolded and unassembled polypeptides, in addition to physiologically regulating the abundance of normal protein in the ER (4, 6). In

this regard, the inhibition of ERAD by the restoration of SVIP expression in BB30-HNC cancer cells was accompanied by the accumulation of polyubiquitinated proteins that are not degraded (Figure 4A). However, the set of proteins that are controlled in particular by the SVIP-mediated inhibition of ERAD have not been characterized or studied in the context of cancer cells. We decided to address this issue by taking advantage of our discovery of SVIP epigenetic loss in transformed cells. We carried out stable isotopic labeling of amino acids in cell culture (SILAC) in empty vector–transfected BB30-HNC cells in comparison with SVIP stably transfected BB30-HNC cells to identify proteins whose expression levels were SVIP dependent (Figure 4B). At the level of resolution used in the SILAC assay, we observed 124 proteins with significantly different expression upon SVIP transfection in BB30-HNC cells (Supplemental Table 1). Most proteins (88%, 110 of 124) showed upregulation upon the recovery of SVIP expression, whereas the other 12% (14 of 124) were downregulated (Figure 4C and Supplemental Table 1). These results fit with the idea that the restoration of SVIP, due to its activity as an ERAD inhibitor, enhances protein levels. In this regard, we found that SVIP transfection upregulated the protein levels of known ERAD targets (32) without increasing the levels of the corresponding RNA transcripts (Figure 4D), as expected. We performed a Gene Ontology (GO) analysis to classify the 110 proteins upregulated upon SVIP transfection in all biological process categories. Metabolic process (GO: 0008152) was the third category represented from the most general classification of biological process, according to the GO Consortium (33). However, most importantly, a deeper analysis of all biological processes in GO revealed that 9 out of 10 more significantly overrepresented categories belonged to the metabolic process subgroup (Figure 4E), particularly for components of mitochondrial metabolism. We selected illustrative targets of these pathways identified as upregulated by SVIP in the SILAC approach (Supplemental Table 1), such as SUCLG2 (tricarboxylic acid cycle), NDUFB8 (oxidative phosphorylation), MT-CO2 (oxidative phosphorylation), and SLC25A5 (mitochondrial carrier) for Western blot and qPCR assays. We confirmed that their SVIP-mediated upregulation occurred at the protein level and was not associated with a difference in RNA levels (Figure 4F), consistent with the proposed role of SVIP as an ERAD inhibitor.

Among the few downregulated proteins observed following SVIP transfection (Supplemental Table 1), we found the glucose transporter 1 (GLUT1), also known as SLC2A1, a glucose transporter that constitutes a rate-limiting step of glucose metabolism and whose overexpression in tumors is associated with increased aerobic glycolysis (16, 34). Western blot confirmed its loss in SVIP-transfected BB30-HNC (Figure 4G), BHY (Supplemental Figure 5A), and Ca-Ski (Supplemental Figure 5A) cells, but we also found decreased levels of its transcript (Figure 4G and Supplemental Figure 5A), so a compensatory mechanism associated with the emergence of mitochondrial metabolism proteins upon SVIP restoration might occur instead of being a direct effect of SVIP on its protein degradation. In this regard, we found that SVIP promoter CpG island hypermethylation was also associated with the downregulation of the GLUT1 transcript in the Sanger panel of cancer cell lines (15) (Figure 4H), being more significant for the 4 tumor types more methylated at the SVIP locus (Figure 4H). SVIP downregulation was also associated with low levels of the GLUT1 transcript in the same panel of cell lines (Supplemental Figure 5B). SVIP methylation–associated silencing is also associated with high levels of expression of the glycolytic enzyme hexokinase 1 and low levels of the uncoupling mitochondrial enzyme UCP2 (Supplemental Figure 5C). Overall, the picture that emerges indicates that SVIP reintroduction caused an enrichment of mitochondrial metabolism compared with SVIP epigenetically deficient cancer cells.

The scenario described above made us wonder whether SVIP hypermethylation–associated silencing could mediate the common metabolic shift of cancer cells that move away from oxidative phosphorylation toward aerobic glycolysis, a phenotype known as the Warburg effect (34, 35). To address this question, we performed a comprehensive set of biochemical and cellular assays. We found that SVIP-transfected BB30-HNC cells experienced reduced cellular glucose uptake in comparison with empty vector–transfected cells (Figure 5A), a finding that relates to the aforementioned SVIP-associated downregulation of GLUT1. In this regard, a common characteristic of tumoral cells is the enhanced dependence on glucose to boost aerobic glycolysis, which produces a large amount of lactate. We found that the restoration of SVIP activity in the epigenetically silenced cells decreased lactate levels (Figure 5B), suggesting that the glycolytic pathway is depleted. In addition, SVIP stably transfected cells exhibited a higher basal oxygen consumption rate (OCR), and had enhanced ATP-linked OCR and maximal OCR compared with empty vector–transfected BB30-HNC cells (Figure 5C), indicating a shift from aerobic glycolysis to oxidative phosphorylation on SVIP recovery. As further evidence of this, ATP levels were higher in the SVIP-transfected BB30-HNC cells (Figure 5D). MitoSox median fluorescence intensity (MFI) determined by flow cytometry showed an increase of mitochondrial
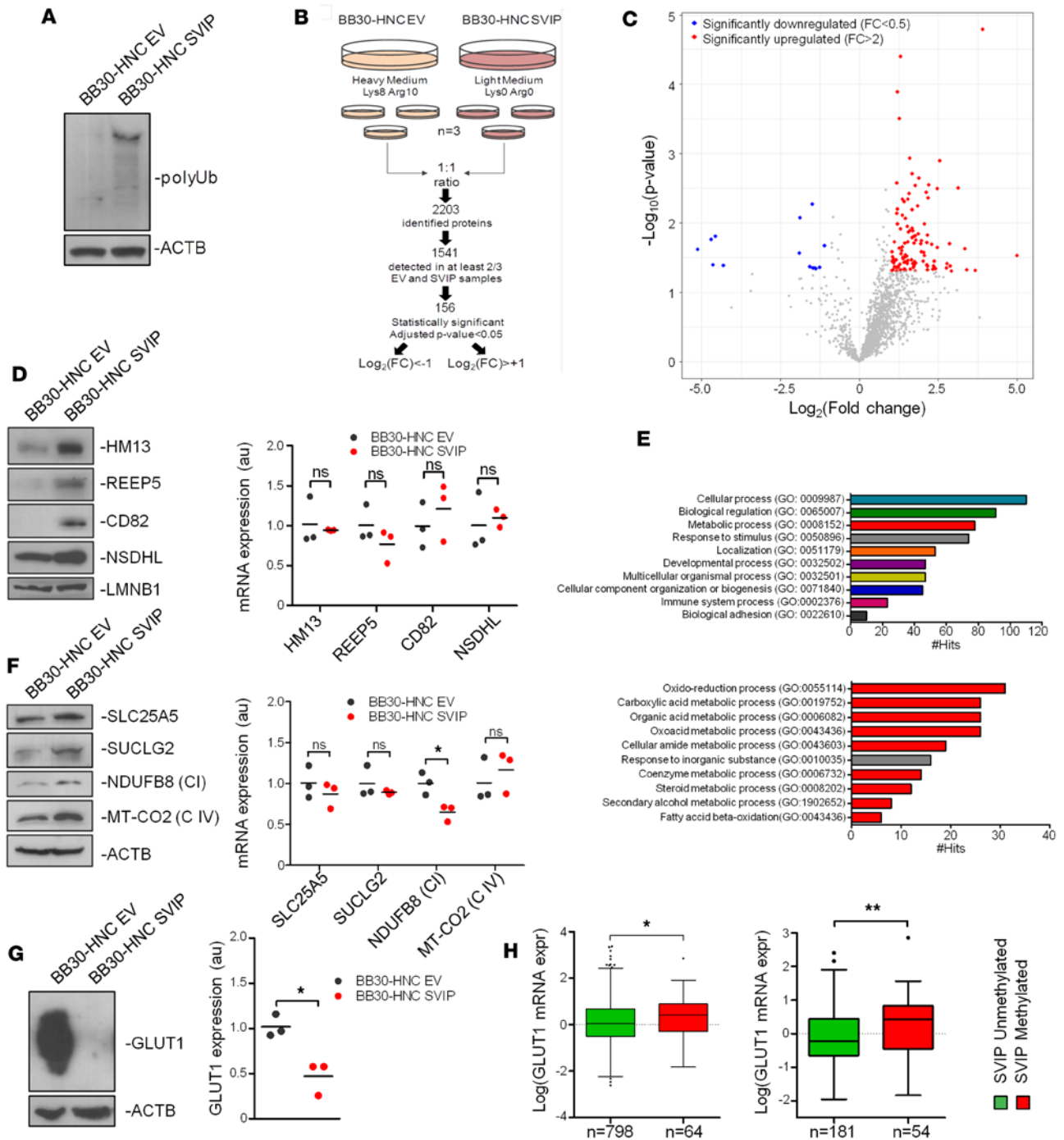
Figure 4. Recovery of SVIP expression in cancer cells upregulates mitochondrial metabolism proteins and downregulates a glucose uptake protein. (**A**) Representative Western blot showing the accumulation of polyubiquitinated proteins after SVIP recovery in BB30-HNC cells. (**B**) Workflow of the SILAC developed to detect protein changes in BB30-HNC cells upon SVIP transfection. (**C**) Volcano plot summarizes the SILAC results. One hundred ten proteins were significantly upregulated ($P < 0.05$) (red dots), whereas only 14 were downregulated (blue dots). (**D**) Validation by Western blot (left) of the upregulation of 4 ERAD target proteins upon transfection of the ERAD inhibitor SVIP. mRNA levels determined by qPCR (right) do not change upon SVIP restoration. (**E**) Top: Number of proteins represented in general gene clusters of Biological Process Gene Ontology enriched with FDR < 0.05. Bottom: Number of proteins represented in top 10 nonredundant clusters of Biological Process Gene Ontology according to their significance (FDR). Colors depict the level 1 Biological Process category in which they are included according to the top panel of Figure 4D. (**F**) Western blot (left) shows upregulation of 4 mitochondrial metabolism proteins upon recovery of SVIP in BB30-HNC cells. mRNA levels determined by qPCR (right) do not change upon SVIP transfection. (**G**) Recovery of SVIP activity causes downregulation of GLUT1 at the protein (left) and mRNA (right) levels, as determined by Western blot and qPCR, respectively. (**H**) *SVIP* promoter hypermethylation is significantly associated with loss of the GLUT1 transcript in the Sanger panel of cancer cell lines ($n = 862$) (left); this correlation was stronger when considering only head and neck cancer, esophageal, cervical, and hematological cell lines ($n = 235$) (right). Two-tailed Mann-Whitney U test was performed to compare GLUT1 expression between methylated and unmethylated cell lines. qPCRs were analyzed using 2-tailed Student's t test, and are represented as the mean of triplicates. All Western blots in panels **A**, **D**, **F**, and **G** were performed in triplicate. *$P < 0.05$; **$P < 0.01$. ns, not significant.

ROS upon SVIP restoration (Figure 5E). MitoTracker MFI probe revealed an increase in mitochondrial mass (Figure 5F). Importantly, SVIP-transfected BHY and Ca-Ski mimicked the phenotype observed for SVIP recovery in BB30-HNC cells; SVIP restoration enhanced ATP levels (Supplemental Figure 5D) and increased mitochondrial mass determined by the MitoTracker probe (Supplemental Figure 5E). Finally, to further elucidate the identified SVIP metabolic shift, we performed isotopologue enrichment analysis using uniformly labeled glucose (U-$^{13}C_6$-glucose), followed by mass spectrometric quantification. This approach demonstrated, again, the greater use of the tricarboxylic acid (TCA) cycle upon SVIP restoration. The detailed isotopologue enrichment analysis also showed an increase in carbon contribution to succinate and citrate in SVIP-transfected cells. Major proportions of M4 and M6 citrate and M2 and M4 succinate in SVIP-transfected cells revealed a higher glucose flux into the mitochondria (Figure 5G).

Our greatest interest was whether the metabolic dependence of SVIP epigenetically deficient cancer cells on glucose, described above, could be exploited for therapeutic purposes. To address this, we first examined whether SVIP expression levels affected cancer cell glucose-dependent growth. We found that BB30-HNC empty vector–transfected cells were unable to grow in media with a low glucose content, but the recovery of SVIP expression allowed the growth of these cells in the glucose-depleted context (Figure 5H). We then continued the study in a pharmacological context using Bay-876, a recently developed specific inhibitor for GLUT1 (36), the protein responsible for glucose uptake that we found upregulated in SVIP epigenetically deficient cells (Figure 4G). Bay-876 displays high selectivity for GLUT1 in comparison with other glucose transporters such as GLUT2, GLUT3, and GLUT4 (36). We first assessed in our panel of cancer cell lines whether DNA methylation–associated silencing of SVIP was associated with different sensitivity to Bay-876. The determination of the corresponding IC_{50} values, according to the SRB assay for cell viability, showed that SVIP epigenetically deficient cancer cells were significantly more sensitive to the specific GLUT1 inhibitor than the SVIP-unmethylated cell lines (Fisher's exact test, $P < 0.05$) (Figure 5I). Furthermore, the restoration of SVIP activity in the epigenetically deficient cancer cells rendered resistance to Bay-876 (Figure 5J) in comparison with the empty vector–transfected cells, which were very sensitive to the small-drug-mediated blockage of glucose uptake. We translated these results to the in vivo setting where we assessed the effect of Bay-876 in subcutaneous xenografted tumors in nude mice. No evident general toxicity was observed in these mice, in agreement with other previously analyzed animal models such as rat and dog (36). Importantly, we found that tumors derived from SVIP-hypermethylated cancer cells were significantly sensitive to growth inhibition upon Bay-876 use, whereas tumors derived from cancer cells where we had restored SVIP expression showed resistance to the compound (Figure 5K).

Overall, the data indicate that cancer cells harboring DNA methylation–associated loss of SVIP are dependent on glucose and aerobic glycolysis to obtain the cellular energy necessary for their survival, whereas SVIP restoration promotes the use of the homeostatic mitochondrial respiration. Interestingly, the extremely high dependence on glucose of those cancer cells with epigenetic loss of SVIP pinpoints a possible therapeutic opportunity for the use of glucose uptake blockers in the management of these tumors.

SVIP epigenetic loss in primary tumors is associated with GLUT1 upregulation and poor clinical outcome. The presence of SVIP promoter CpG island hypermethylation was not confined to established cancer cell lines, but was also observed in primary human malignancies. Data-mining of the set of primary human tumors from The Cancer Genome Atlas (TCGA) project (https://cancergenome.nih.gov/), interrogated by the same DNA methylation microarray used herein (37), demonstrated the occurrence of 5′-end CpG island hypermethylation of the SVIP gene in a wide spectrum of tumor types that was similar to the profile observed in the cancer cell line data (Figure 6A). In this regard, SVIP CpG island promoter hypermethylation was frequently found in head and neck (37%, 184 of 496), cervical (19%, 60 of 309), and esophageal (10%, 18 of 183) tumors (Figure 6A). As we also studied the cancer cell lines, we were able to compare the described TCGA profile of SVIP CpG island methylation with the available RNA data. We found that SVIP CpG island promoter hypermethylation was associated with downregulation of its transcript for the described tumor types (Figure 6B), further reinforcing the link between aberrant DNA methylation and transcriptional inactivation of the gene. As it occurred in the in vitro models, SVIP downregulation was associated with the overexpression of ER stress markers such as XBP1 and DERL3 (Supplemental Figure 6A). Interestingly, as previously noted in the cancer cell lines (Figure 4G), SVIP CpG island hypermethylation in the TCGA primary tumors was also associated with overexpression of the GLUT1 transcript (Figure 6C). SVIP downregulation is also associated with low levels of GLUT1 (Supplemental Figure 6B), the glycolytic enzyme HK1, and the mitochondrial protein UCP2 (Supplemental Figure 6C) among the TCGA samples. These results highlight the connection between SVIP epigenetic inactivation and glycolysis dependence.
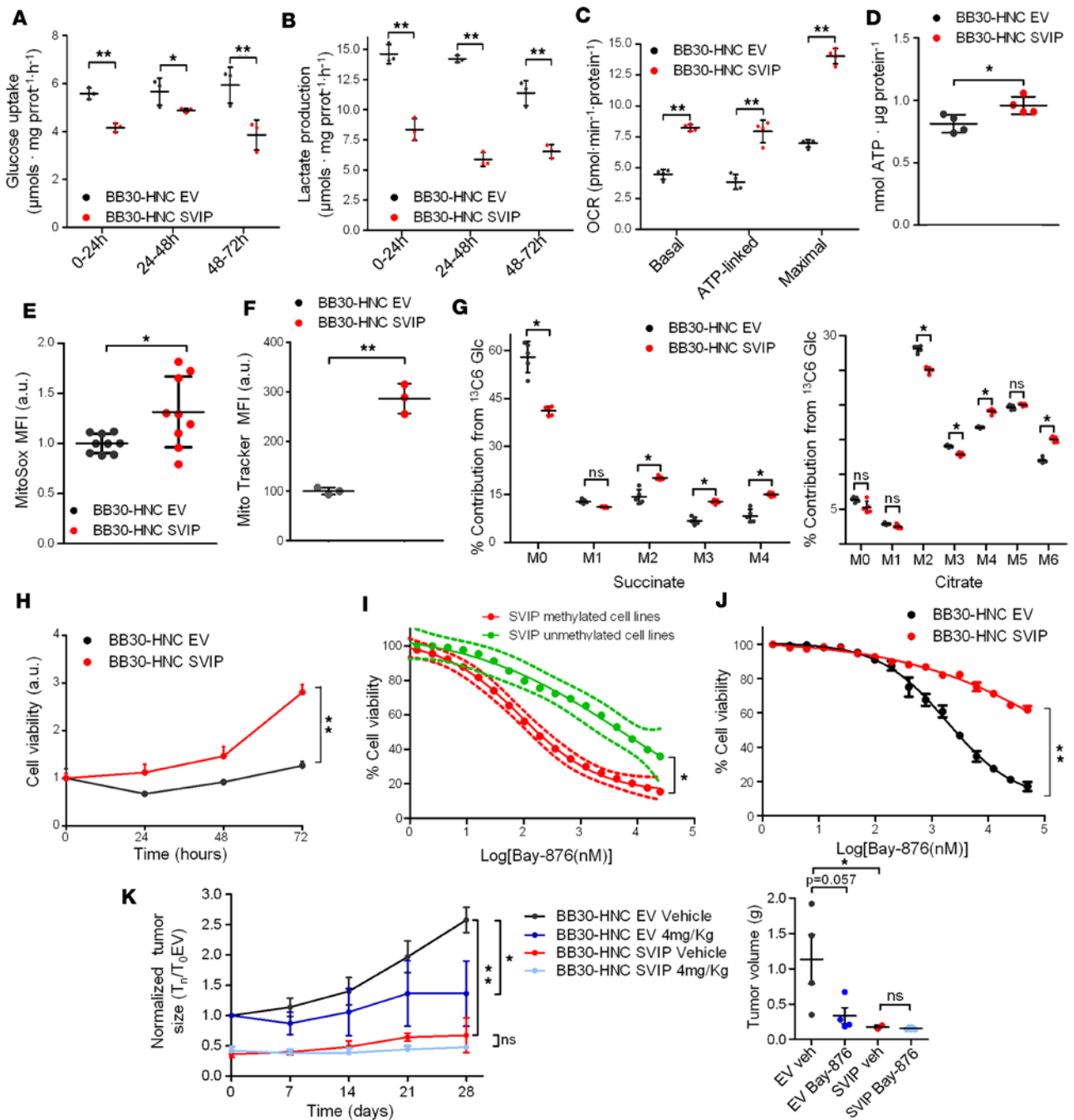
Figure 5. Restoration of SVIP expression in transformed cells shifts an aerobic glycolysis phenotype to homeostatic mitochondrial metabolism. Enzymatic determination of (**A**) glucose uptake and (**B**) lactate release normalized with respect to protein concentration in empty vector– and SVIP-transfected BB30-HNC cells. Graphs are representative of 3 independent experiments. Data were analyzed through 2-tailed Student's *t* test. (**C**) Oxygen consumption rate (OCR) normalized with respect to protein concentration of empty vector– and SVIP-transfected BB30-HNC cells under basal conditions (Basal), after oligomycin treatment (ATP-linked), and after FCCP injection (Maximal OCR). This graph is representative of 2 independent experiments, each with 5 technical replicates. (**D**) ATP concentration determination in empty vector– and SVIP-transfected BB30-HNC cells. Graph is representative of 3 independent experiments. (**E**) MitoSox median fluorescence intensity (MFI) was determined by flow cytometry. Nine replicates of 4 independent experiments are plotted. (**F**) MitoTracker MFI was determined by flow cytometry. Mean ± SD of a representative experiment is shown. (**G**) ^{13}C-citrate and ^{13}C-succinate isotopologue distribution after 24-hour exposure to 25 mM $^{13}C_6$-glucose. (**H**) BB30-HNC cell growth in 5 mM low-glucose medium. Graph is representative of 3 independent experiments. (**I**) SRB assays to determine cell viability upon the use of Bay-876 (GLUT1 inhibitor) of 4 SVIP-unmethylated and -expressing cell lines (green) against 5 cell lines with SVIP hypermethylation–associated silencing (red). (**J**) SRB assay shows that empty vector–transfected cells with SVIP epigenetic loss are significantly more sensitive to growth inhibition by Bay-876 treatment than are cancer cells with transfection-mediated recovery of SVIP expression. Graph is representative of 3 independent experiments. Statistical differences were determined by Student's *t* test at the highest dose. (**K**) Growth inhibition of empty vector– and SVIP-transfected BB30-HNC cells in an in vivo subcutaneous mouse model was measured by tumor volume time course (left) and final tumor weight (right). Statistical differences in **I** and **K** were determined by adjusting the curves to third-grade polynomial equations followed by the extra sum-of-squares *F* test. *$P < 0.5$, **$P < 0.01$. ns, not significant.

Finally, we wondered whether SVIP hypermethylation was of any prognostic value with respect to the tumor suppressor capacity of the protein, described above. To address this question, we compared the SVIP methylation status of the primary head and neck tumors derived from TCGA with the available clinicopathological data (n = 282 samples), being the tumor type that most often experiences SVIP epigenetic inactivation (Figure 1A and Figure 6A). SVIP hypermethylation was associated with shorter disease-free survival (DFS) (log-rank; P = 0.024; hazard ratio [HR] = 1.65, 95% CI = 1.07–2.55) and worse overall survival (OS) (log-rank; P = 0.020; HR = 1.66, 95% CI = 1.08–2.57) in the head and neck cancer TCGA cohort (Figure 6D). Low SVIP expression was also associated with shorter DFS and worse OS (Supplemental Figure 6D), but GLUT1 expression did not associate with clinical outcome (Supplemental Figure 6E). Low SVIP expression was also associated with high expression of the proliferation marker CCND1 (Supplemental Figure 6F). We did not find any associations between SVIP hypermethylation and the clinicopathological variables, except the histological classification, where SVIP hypermethylation was more common in head and neck carcinomas of the squamous type (Supplemental Table 2). Furthermore, multivariate Cox regression analysis showed that SVIP hypermethylation was an independent predictor of shorter OS (HR = 1.61, P = 0.034; 95% CI = 1.04–2.51), in comparison with all other patient characteristics, for the interrogated TCGA cohort of head and neck cancer cases (Figure 6E). This implies that the epigenetic inactivation of SVIP is a potential prognostic marker of poor outcome for these malignancies.

Discussion

Cancer cells must overcome intracellular proteotoxic and metabolic stress, in addition to a hostile microenvironment, to survive and proliferate. To adapt, transformed cells rely on hijacking the protein quality controls of the ER, such as the adequate protein folding, the UPR, and the ERAD pathways. The latter network, which has targets such as the tumor suppressor p53 (38), not only acts as a quality control mechanism that clears the ER of unfolded proteins, but also regulates protein abundance (6, 39). In the current study, we have shown that a major mechanism used by common human tumors to influence the ERAD pathway occurs by promoter CpG island hypermethylation–associated silencing of the ERAD inhibitor SVIP. The epigenetic loss of this interactor of AAA-ATPase VCP/p97, the enzyme responsible for retrotranslocation of ERAD substrates across the ER membrane, is an effective way of dealing with potentially excessive ER stress in the tumor types examined here. Restoration of the SVIP protein induces major ER stress that blocks the growth of these cancer cells, rendering them sensitive to drugs that lead to the accumulation of unfolded proteins such as SERCA inhibitors (29–31). Related to its ERAD inhibitor role, we observed that the recovery of SVIP expression induced an increase in the expression levels of many proteins. Interestingly, many of the proteins that become upregulated upon SVIP activation are required for mitochondrial metabolism, suggesting an important role for SVIP in the regulation of cancer cell metabolism.

One of the most common traits of human tumors is the presence of the Warburg effect (34, 35), characterized by aerobic glycolysis. This metabolic phenotype is characterized, among other features, by increased glucose uptake and lactate production regardless of oxygen concentration, an enhanced rate of glycolysis, and a reduced level of oxidative phosphorylation via the tricarboxylic acid (TCA) cycle (34, 35). Although the energetic production of aerobic glycolysis is much lower than that of oxidative phosphorylation, this shift seems to be positively selected in cancer cells due to its production of growth-promoting glucose metabolites and enhanced nonoxidative ATP generation (40). Cancer cells come to express the Warbug effect by acquiring various genetic and epigenetic changes (34, 35, 40). Our results indicate that SVIP epigenetic silencing is a frequent method by which the tumor types considered accomplish that goal. Cancer cells with SVIP hypermethylation–associated silencing are characterized by increased glucose uptake and lactate production, decreased mitochondrial mass and activity, and a greater dependence on glucose. However, the restoration of the SVIP protein reverts the Warburg phenotype to one of physiological mitochondrial respiration.

Most importantly from the translational standpoint, cancer cells carrying the SVIP epigenetic defect have high levels of GLUT1, the protein responsible for the intracellular uptake of glucose, in cell lines and primary tumors, whereas in vitro these cells are highly dependent on glucose for their growth. Remarkably, tumoral cells with SVIP hypermethylation are very sensitive to a newly designed small molecule, Bay-876, that is a specific inhibitor of GLUT1 (36), whereas the recovery of SVIP expression produces resistance to this drug. These findings could be extremely significant in the clinical context, because human tumors that overexpress GLUT1 are usually associated with the poor outcome of patients (41, 42). In this regard, we have noted the same phenomenon, whereby primary tumors with the
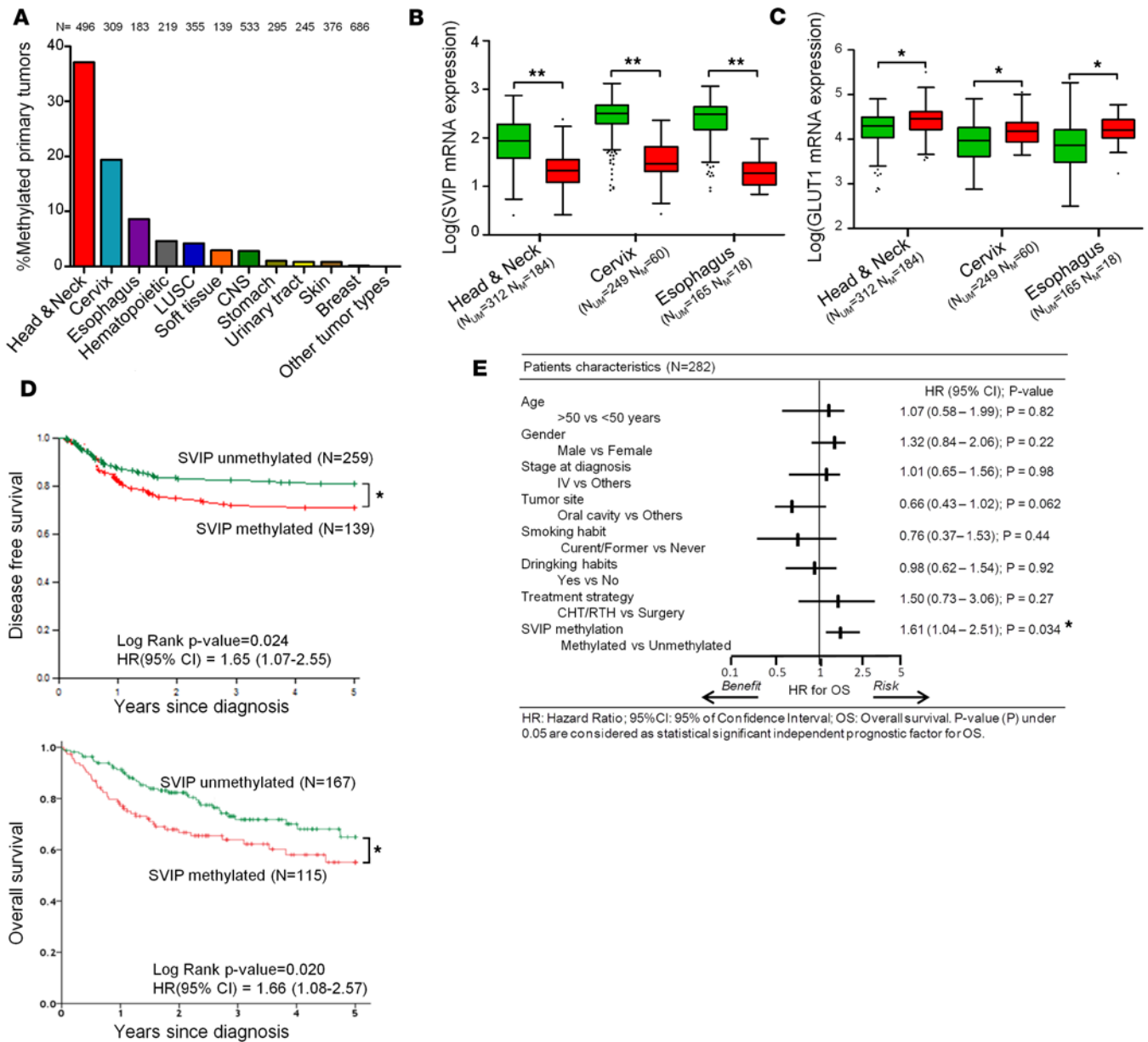
Figure 6. *SVIP* epigenetic inactivation in human primary tumors and its association with poor clinical outcome. (**A**) Percentage of *SVIP* methylation in the TCGA data set of primary tumors by cancer type. Samples were considered hypermethylated with a β value higher than 0.33. (**B**) *SVIP* promoter CpG island methylation is associated with the loss of the *SVIP* transcript among head and neck, cervical, and esophageal primary tumors in the TCGA data set. Two-tailed Mann-Whitney *U* test was performed. (**C**) *SVIP* hypermethylation is associated with a high level of expression of the *GLUT1* transcript among head and neck, cervical, and esophageal primary tumors in the TCGA data set. (**D**) Kaplan-Meier analysis of DFS (top) and OS (below) by *SVIP* methylation status in head and neck primary tumors of the TCGA data set. The *P* value corresponds to the log-rank test. Results of the univariate Cox regression analysis are represented by the hazard ratio (HR) and 95% confidence interval (CI). (**E**) Multivariate Cox regression analysis of OS, represented by a forest plot, taking into account the clinical characteristics of the TCGA cohort of head and neck cancer patients. In multivariate analyses, significant covariates are considered independent prognostic factors of clinical outcome; this was the case for *SVIP* methylation. *$P < 0.05$; **$P < 0.01$.

SVIP epigenetic alteration have the shortest OS. These observations justify the increasing efforts to find small-molecule inhibitors of GLUT1 (42) and to explore the potential therapeutic benefit of the blockage of this transporter. The appropriate selection of the tumors treated with the GLUT1 inhibitor could be critical to avoiding excessive toxicity because this protein is expressed in all normal tissues in order to maintain the basal glucose supply (43). Patients with tumors exhibiting SVIP epigenetic loss and an associated "addiction" to aerobic glycolysis, glucose, and GLUT1, are likely to respond better in future clinical trials designed to validate the genuine therapeutic benefits of these types of drugs.

Methods

Cell lines and primary tumor samples. Cancer cell lines were purchased from the American Type Culture Collection (ATCC) (Ca-Ski, HeLa, and SW756), the German Collection of Microorganisms and Cell Cultures (DSMZ) (BHY, COLO-680N and KYSE-180), and Sigma-Aldrich (OACM 5.1C). Lb771-HNC, Ca9-22, and BB30-HNC were kindly provided by the Sanger Institute. The head and neck cancer cell lines were cultured in Dulbecco's Modified Eagle's Medium (DMEM) supplemented with 10% fetal bovine serum (FBS) and 1% penicillin/streptomycin antibiotic at 37°C and 5% CO_2. Cervical and esophageal cell lines were cultured in Roswell Park Memorial Institute (RPMI1640) medium supplemented with 10% FBS and 1% penicillin/streptomycin antibiotic at 37°C and 5% CO_2. DNA methylation and clinical information about patients with primary tumors was obtained from the TCGA database by using the cgds-R package and the cBioPortal website (https://www.cbioportal.org/).

DNA methylation analysis. DNA methylation profiles were obtained by bisulfite genomic sequencing. CpG islands were identified in silico using Methyl Primer Express v1.0 (Applied Biosystems). Genomic DNA was converted using the EZ DNA Methylation-Gold Kit (ZYMO Research). Bisulfite PCR products were transformed into competent bacteria. At least 8 clones were sequenced to calculate the methylation frequency. Sequence reads were aligned using BioEdit software and promoter methylation was represented using BSMap software. Bisulfite sequencing primers are listed in the Key Resources Table in the supplemental material. The DNA methylation microarray used was the Infinium HumanMethylation450 BeadChip (Illumina). In silico DNA methylation analysis of VCP/p97, SELENOS, SYVN1, SVIP, and AMFR/GP78 was performed using CpG sites located in the corresponding 5′-end regulatory regions (listed in Dataset 1). The threshold to define "methylated" was an average of the interrogated CpG β values ≥ 0.66.

Expression analysis. Total RNA was extracted from cell lines using the cell lysate program for the Maxwell 16 instrument (Promega). RNA (2 μg) was retrotranscribed using GoScript (Promega). qPCR reactions were performed using SYBR Green PCR Master Mix (Thermo Fisher Scientific) in a QuantStudio 5 Real-Time PCR System (Thermo Fisher Scientific). Data were normalized using GAPDH as an endogenous control. qPCR primers are listed in the Key Resources Table in the supplemental material. Total protein extracts were obtained using RIPA buffer (20 mM Tris-HCl [pH 7.5], 150 mM NaCl, 1 mM Na_2EDTA, 1 mM EGTA, 1% NP-40) and quantified using the DC Protein Assay (Bio-Rad). Protein levels were analyzed by Western blot using β-actin (ACTB), α-tubulin (TUBA), or lamin B1 (LMNB1) as the loading control. Specific primary and secondary antibodies against target proteins are listed in the Key Resources Table in the supplemental material.

Modulation of in vitro SVIP expression. The *SVIP* cDNA sequence was subcloned into the pLVX-IRES-ZsGreen 1 expression vector (Clontech). The forward primer contained a Kozak consensus sequence, which promotes flexible transcript translation. Four shRNAs designed with *rnaidesigner* (Thermo Fisher Scientific) were subcloned into the pLVX-shRNA2 vector. Empty pLVX-IRES-ZsGreen 1 and shRNA against the MSS2 yeast mRNA (not present in mammals) were used as a control in overexpression and depletion models, respectively. Plasmids were transfected in HEK-293T cells using jetPRIME Transfection Reagent (Polyplus Transfection), together with psPAX2 (Addgene) and pMD2.G (Addgene) packaging plasmids. After 72 hours, the lentiviral supernatant medium was collected and 0.45-μm filtered. Cell lines were cultured in the medium containing the appropriate virus for 24 hours. After 5 passages, ZsGreen 1–positive cells were sorted by FACS.

Imaging. For TEM, cancer cells were fixed in 2.5% glutaraldehyde in 0.1 M phosphate buffer, postfixed in 1.5% osmium tetroxide, and processed using the tEPON 812 embedding Kit (Tousimis). The ultrathin sections, stained with uranyl acetate and lead citrate, were assessed at 80 kV with a JEM-1011 (JEOL) transmission electron microscope. For senescence-associated β-galactosidase staining, BB30-HNC cells were fixed with 2% v/v paraformaldehyde and 0.2% v/v glutaraldehyde and stained (40 mM citric acid phosphate pH 6.0, 150 mM NaCl, 5 mM $K_3Fe[CN]_6$, $K_4Fe[CN]_6$, 2 mM $MgCl_2$, and 1 mg/ml X-Gal solution) for quantifying senescent cells.

Cell viability and drug-dose response assays. Cell viability was assessed by the SRB assay. Cells per well were seeded at 1,000 cells/well in 96-well plates. On 7 consecutive days, cells were fixed with 10% trichloroacetic acid, washed, then stained with the SRB dye. Cell viability was assessed by measuring absorbance at 540 nm. For the glucose-dependent cell viability assay, 2,000 cells per well were seeded in 96-well plates and grown in glucose-, pyruvate-, and glutamine-free media supplemented with dialyzed FBS, 1 mg/ml glucose, and 4 mM glutamine. Medium was changed every 24 hours to avoid nutrient depletion. The SRB assay was carried out

at 0, 24, 48, and 72 hours. For drug dose-response assays, 5,000 cells per well were plated in 96-well plates and treated with different doses of the appropriate drug after overnight cell adherence. The SRB assay was performed after 96 hours. Bortezomib was purchased from LC Laboratories. 17-AAG, Eeyarestatin I, Bay-876, and thapsigargin were purchased from Sigma-Aldrich. IPI-504 was purchased from Medchem.

In vivo experiments. Empty vector–transfected or SVIP-transfected BB30-HNC cells (3.5×10^6) were injected into the left and right flanks, respectively, of nude male mice. Tumor growth was monitored every 2 days by measuring its width (W) and length (L). Tumor volume, V, was estimated using the formula $V = \pi/6 \times L \times W^2$. Mice were sacrificed 80 days after injection and their tumor weight measured. Bay-876 was administered orally at 4 mg/kg dissolved in 1:9 NMP/PEG (1-methyl-2-pyrolidinone/poly [ethylene glycol] 300).

Cytometry analyses. Mitochondrial ROS were measured using red MitoSox probe (Thermo Fisher Scientific). Mitochondrial mass was measured using deep-red MitoTracker probe (Thermo Fisher Scientific). Cultured cells were incubated with the aforementioned probe for 30 minutes and then analyzed with a FACSCalibur (Beckton Dickinson).

SILAC labeling and liquid chromatography–mass spectrometry analysis. SILAC labeling was performed using SILAC Lys(8) Arg(10) Kit medium (Silantes). Empty vector– and SVIP-transfected BB30-HNC cells were grown for 10 days in heavy medium [Lys(8), Arg(10)] or light medium [Lys(0), Arg(0)]. After labeling, protein was extracted by using RIPA buffer. Protein levels were quantified by Lowry and mixed at a 1:1 ratio. Samples were further processed by the FASP method followed by alkylation with iodoacetamide and overnight digestion by Lys-C and trypsin at 37°C in 50 mM ammonium bicarbonate. Peptide mixes were analyzed using an Orbitrap Fusion Lumos mass spectrometer (Thermo Fisher Scientific) coupled to an EasyLC (Thermo Fisher Scientific). All data were acquired with Xcalibur software v3.0.63. The Proteome Discoverer software suite (v2.0, Thermo Fisher Scientific) and the Mascot search engine (v2.5, Matrix Science) were used to identify and quantify peptides. Samples were searched against a Swiss-Prot database containing entries corresponding to Human (https://www.uniprot.org/peptidesearch/, April 2016 version), a list of common contaminants, and all the corresponding decoy entries. Resulting data files were filtered for FDR < 1%.

Gene functional enrichment analysis. Gene sets were used to analyze gene set overrepresentation in the GO biological processes included in the PANTHER web service (http://www.pantherdb.org/). The general categories and top gene clusters resulting from the hypergeometric test with an FDR-adjusted *P* value < 0.05 were subsequently considered.

Metabolic determinations. Oxygen consumption and pH variation were determined using an XF24 extracellular flux analyzer (Seahorse Bioscience). Those variables were measured under routine conditions (DMEM plus 5.5 mM glucose) and after the sequential addition of 1 μg/ml oligomycin (Complex V inhibitor), 1.5 μM FCCP, and 0.1 μM rotenone and antimycin A. All substrates, uncouplers, and inhibitors were purchased from Sigma-Aldrich. Concentrations of glucose and lactate in growth medium were determined by enzymatic assays. After overnight cell adherence, medium was collected and replaced every 24 hours. Glucose concentration was calculated by coupling hexokinase and glucose-6-phosphate dehydrogenase enzymatic reactions. Lactate concentration was determined by its conversion to pyruvate by LDH in the presence of hydrazine. In all cases, absorbance at 340 nm was measured using a Cobas Mira Chemical Analyzer (Roche) to assess NADH concentration, which is directly proportional to the given metabolite concentration. Glucose and lactate concentrations at 24, 48, and 72 hours were compared with the concentration at the start time to assess consumption and production, respectively. Data were normalized by SRB assay of the cultured cells. ATP production was calculated using CellTiter-Glo (Promega) according to the manufacturer's indications. Absolute ATP concentration was calculated using the dATP standard curve following the Beer-Lambert law.

Metabolic flux analysis. Cells were cultured for 24 hours in the presence of fully labeled glucose ($^{13}C_6$-glucose, Sigma-Aldrich). Then, cell pellets were scraped, collected, and frozen. Briefly, cell pellets were resuspended with 450 μl of cold methanol/water (8:1, v/v) containing ^{13}C-glycerol (5 ppm) as internal standard. Metabolite lysates were purified with 3 rounds of liquid nitrogen immersion and sonication, followed by 1 hour in ice before centrifugation (5000 *g*, 15 minutes at 4°C). Samples were dried under a stream of N_2 gas and lyophilized before chemical derivatization with 12 μl methoxyamine in pyridine (40 μg/μl) for 45 minutes at 60°C. Samples were also sialylated using 8 μl *N*-methyl-*N*-trimethylsilyltrifluoroacetamide with 1% trimethylchlorosilane (Thermo Fisher Scientific) for 30 minutes at 60°C to increase the volatility of metabolites. A 7890 GC system coupled to a 7000 QqQ mass spectrometer (Agilent Technologies) was used for isotopologue determination. Derivatized samples (1 μl) were injected into the gas chromatograph system with a split inlet equipped with a J&W Scientific DB5−MS+DG stationary phase column (30 mm × 0.25

mm i.d., 0.1 μm film, Agilent Technologies). Helium was used as the carrier gas. Metabolites were ionized using positive chemical ionization (CI) with isobutene as reagent gas. Mass spectral data on the 7000 QqQ were acquired in scan mode, monitoring selected ion clusters of the various metabolites.

Statistics. The associations between variables were assessed by Welch's *t* test, Student's *t* test, the Wilcoxon paired test, or Spearman's correlation as appropriate. Kaplan-Meier plots and log-rank tests were used to estimate OS. Statistical analyses were carried out with IBM SPSS for Windows and GraphPad Prism 5 for Windows. Values of $P < 0.05$ were considered statistically significant. All statistical tests were 2-sided.

Study approval. All animal studies were approved by and conducted in accordance with the guidelines established by the IDIBELL Animal Research Ethics Committee (procedure number 3880).

Author contributions

Acknowledgments

Address correspondence to: Manel Esteller, Bellvitge Biomedical Research Institute (IDIBELL), Avinguda Gran Via de l'Hospitalet, 199, Hospital Duran i Reynals, 3rd floor, Cancer Epigenetics and Biology Program (PEBC) L'Hospitalet (Barcelona) 08908, Spain. Phone: 34.93.2607253; Email: mesteller@carrerasresearch.org.

1. Gandolfi S, Laubach JP, Hideshima T, Chauhan D, Anderson KC, Richardson PG. The proteasome and proteasome inhibitors in multiple myeloma. *Cancer Metastasis Rev*. 2017;36(4):561–584.
2. Bravo R, et al. Endoplasmic reticulum and the unfolded protein response: dynamics and metabolic integration. *Int Rev Cell Mol Biol*. 2013;301:215–290.
3. Wang M, Kaufman RJ. The impact of the endoplasmic reticulum protein-folding environment on cancer development. *Nat Rev Cancer*. 2014;14(9):581–597.
4. Hwang J, Qi L. Quality control in the endoplasmic reticulum: crosstalk between ERAD and UPR pathways. *Trends Biochem Sci*. 2018;43(8):593–605.
5. Almanza A, et al. Endoplasmic reticulum stress signalling - from basic mechanisms to clinical applications. *FEBS J*. 2019;286(2):241–278.
6. Vembar SS, Brodsky JL. One step at a time: endoplasmic reticulum-associated degradation. *Nat Rev Mol Cell Biol*. 2008;9(12):944–957.
7. Anderson DJ, et al. Targeting the AAA ATPase p97 as an approach to treat cancer through disruption of protein homeostasis. *Cancer Cell*. 2015;28(5):653–665.
8. Bastola P, Neums L, Schoenen FJ, Chien J. VCP inhibitors induce endoplasmic reticulum stress, cause cell cycle arrest, trigger caspase-mediated cell death and synergistically kill ovarian cancer cells in combination with Salubrinal. *Mol Oncol*. 2016;10(10):1559–1574.
9. Zhang H, et al. Targeting VCP enhances anticancer activity of oncolytic virus M1 in hepatocellular carcinoma. *Sci Transl Med*. 2017;9(404):eaam7996.

10. Hänzelmann P, Schindelin H. The structural and functional basis of the p97/valosin-containing protein (VCP)-interacting motif (VIM): mutually exclusive binding of cofactors to the N-terminal domain of p97. *J Biol Chem*. 2011;286(44):38679–38690.

11. Ye Y, Shibata Y, Yun C, Ron D, Rapoport TA. A membrane protein complex mediates retro-translocation from the ER lumen into the cytosol. *Nature*. 2004;429(6994):841–847.

12. Tang WK, Zhang T, Ye Y, Xia D. Structural basis for nucleotide-modulated p97 association with the ER membrane. *Cell Discov*. 2017;3:17045.

13. Hwang J, et al. Characterization of protein complexes of the endoplasmic reticulum-associated degradation E3 ubiquitin ligase Hrd1. *J Biol Chem*. 2017;292(22):9104–9116.

14. Ballar P, Zhong Y, Nagahama M, Tagaya M, Shen Y, Fang S. Identification of SVIP as an endogenous inhibitor of endoplasmic reticulum-associated degradation. *J Biol Chem*. 2007;282(47):33908–33914.

15. Iorio F, et al. A Landscape of pharmacogenomic interactions in cancer. *Cell*. 2016;166(3):740–754.

16. Lopez-Serra P, et al. A DERL3-associated defect in the degradation of SLC2A1 mediates the Warburg effect. *Nat Commun*. 2014;5:3608.

17. Esteller M. Epigenetics in cancer. *N Engl J Med*. 2008;358(11):1148–1159.

18. Baylin SB, Jones PA. A decade of exploring the cancer epigenome - biological and translational implications. *Nat Rev Cancer*. 2011;11(10):726–734.

19. Feinberg AP. The Key role of epigenetics in human disease prevention and mitigation. *N Engl J Med*. 2018;378(14):1323–1334.

20. Wang Y, et al. SVIP induces localization of p97/VCP to the plasma and lysosomal membranes and regulates autophagy. *PLoS ONE*. 2011;6(8):e24478.

21. Khodayari N, et al. SVIP regulates Z variant alpha-1 antitrypsin retro-translocation by inhibiting ubiquitin ligase gp78. *PLoS ONE*. 2017;12(3):e0172983.

22. Nagahama M, et al. SVIP is a novel VCP/p97-interacting protein whose expression causes cell vacuolation. *Mol Biol Cell*. 2003;14(1):262–273.

23. Ballar P, Fang S. Regulation of ER-associated degradation via p97/VCP-interacting motif. *Biochem Soc Trans*. 2008;36(Pt 5):818–822.

24. Dou QP, Zonder JA. Overview of proteasome inhibitor-based anti-cancer therapies: perspective on bortezomib and second generation proteasome inhibitors versus future generation inhibitors of ubiquitin-proteasome system. *Curr Cancer Drug Targets*. 2014;14(6):517–536.

25. Wang Q, Li L, Ye Y. Inhibition of p97-dependent protein degradation by Eeyarestatin I. *J Biol Chem*. 2008;283(12):7445–7454.

26. Magnaghi P, et al. Covalent and allosteric inhibitors of the ATPase VCP/p97 induce cancer cell death. *Nat Chem Biol*. 2013;9(9):548–556.

27. Wagatsuma A, et al. Pharmacological targeting of HSP90 with 17-AAG induces apoptosis of myogenic cells through activation of the intrinsic pathway. *Mol Cell Biochem*. 2018;445(1–2):45–58.

28. Di K, et al. Profiling Hsp90 differential expression and the molecular effects of the Hsp90 inhibitor IPI-504 in high-grade glioma models. *J Neurooncol*. 2014;120(3):473–481.

29. Quynh Doan NT, Christensen SB. Thapsigargin, origin, chemistry, structure-activity relationships and prodrug development. *Curr Pharm Des*. 2015;21(38):5501–5517.

30. Duprez J, Jonas JC. Role of activating transcription factor 3 in low glucose- and thapsigargin-induced apoptosis in cultured mouse islets. *Biochem Biophys Res Commun*. 2011;415(2):294–299.

31. Oslowski CM, Urano F. Measuring ER stress and the unfolded protein response using mammalian tissue culture system. *Meth Enzymol*. 2011;490:71–92.

32. Huang EY, et al. A VCP inhibitor substrate trapping approach (VISTA) enables proteomic profiling of endogenous ERAD substrates. *Mol Biol Cell*. 2018;29(9):1021–1030.

33. Ashburner M, et al. Gene ontology: tool for the unification of biology. The Gene Ontology Consortium. *Nat Genet*. 2000;25(1):25–29.

34. Vander Heiden MG, Cantley LC, Thompson CB. Understanding the Warburg effect: the metabolic requirements of cell proliferation. *Science*. 2009;324(5930):1029–1033.

35. Liberti MV, Locasale JW. The Warburg effect: how does it benefit cancer cells? *Trends Biochem Sci*. 2016;41(3):211–218.

36. Siebeneicher H, et al. Identification and optimization of the first highly selective GLUT1 inhibitor BAY-876. *ChemMedChem*. 2016;11(20):2261–2271.

37. Sandoval J, et al. Validation of a DNA methylation microarray for 450,000 CpG sites in the human genome. *Epigenetics*. 2011;6(6):692–702.

38. Yamasaki S, et al. Cytoplasmic destruction of p53 by the endoplasmic reticulum-resident ubiquitin ligase 'Synoviolin'. *EMBO J*. 2007;26(1):113–122.

39. Brodsky JL. Cleaning up: ER-associated degradation to the rescue. *Cell*. 2012;151(6):1163–1167.

40. DeBerardinis RJ, Lum JJ, Hatzivassiliou G, Thompson CB. The biology of cancer: metabolic reprogramming fuels cell growth and proliferation. *Cell Metab*. 2008;7(1):11–20.

41. Szablewski L. Expression of glucose transporters in cancers. *Biochim Biophys Acta*. 2013;1835(2):164–169.

42. Ancey PB, Contat C, Meylan E. Glucose transporters in cancer - from tumor cells to the tumor microenvironment. *FEBS J*. 2018; 285(16): 2926–2943.

43. Gnudi L, et al. GLUT-1 overexpression: Link between hemodynamic and metabolic factors in glomerular injury? *Hypertension*. 2003;42(1):19–24.